Author Query Form

Chapter title: Introduction to Computed Microtomography & Applications in Earth Science

Author: M.L. Rivers

Chapter: 05

The following queries have arisen during copy-editing your manuscript. Please provide an answer in the right-hand column below and on your proofs. Many thanks for your help.

Query No.	Query	Response
Q1	Please confirm author is just two or more than that.	
Q2	Please confirm whether I K should be KI and Cs K should be CsCl?.	
Q3	Please provide editors.	
Q4	Please provide better quality art work for Figures 1 and 24.	

INTRODUCTION TO COMPUTED MICROTOMOGRAPHY AND APPLICATIONS IN EARTH SCIENCE

Mark L. Rivers

Department of Geophysical Sciences and Center for Advanced Radiation Sources, University of Chicago, Building 434A, Argonne National Laboratory, 9700 South Cass Avenue, Lemont, IL 60439, USA
e-mail: rivers@cars.uchicago.edu

Computed X-ray tomography is a technique that produces cross sections of an object from a series of projections at different angles. The technique has found widespread use in medical CAT scanners, which typically have resolutions of ~1 mm. Microtomography is the extension of this technique to smaller spatial resolution down to <1 μm. In the last 15 years the development of high-brightness synchrotron X-ray sources, high-resolution CCD detectors, and high-performance computing have allowed the field of microtomography to progress rapidly. It is now being applied widely in Earth and soil science, where it is used to image the 3-D distribution of minerals, fluids, and pores. By exploiting X-ray absorption edges, 3-D images of the distribution of specific chemical elements can be produced. This is used to image the distribution of aqueous and organic fluids that have been doped with contrast agents such as iodine and cesium. The method is also being used to locate trace-mineral phases containing high-atomic-number elements such as zirconium and cerium. With fluorescence tomography 3-D images of trace element abundances and even oxidation states can be produced. This is being applied to understand the chemical contamination and remediation by plants in the environment. Diffraction tomography images the 3-D distribution of crystalline phases based on their powder diffraction peaks, and is very useful for imaging materials with similar X-ray absorption and composition but different crystalline structures.

1. Introduction to Computed Tomography

1.1. Overview

Computed tomography is a technique which produces a cross-section of an object from a series of projections collected at different angles. The fact that this can be accomplished at all is not intuitively obvious, and the 1979 Nobel Prize in Physiology or Medicine was awarded to Allan Cormack and Godfrey Hounsfield for their invention of the Computer Assisted Tomography (CAT) technique. So-called CAT scanners developed rapidly and have revolutionized medical imaging by quickly providing a series of virtual slices through the body. Medical CAT scanners typically have a resolution of ~0.5–1 mm, which is sufficient for many medical imaging problems.

The most common type of computed tomography is based on X-ray absorption in the sample. When X-rays travel through a sample they are absorbed according to the familiar Beer's law:

$$I/I_0 = \exp^{-\mu t} \tag{1}$$

where I is the transmitted intensity, I_0 is the incident intensity, t is the thickness of the sample, and μ is the linear X-ray absorption coefficient. μ is a function of both the sample material and the X-ray energy. μ depends linearly on the sample density, but is a very strong function of the atomic number of the elements present in the sample. μ decreases rapidly with increasing X-ray energy, except in the region of X-ray absorption edges where there is a sharp increase in μ as the X-ray energy crosses the edge.

In addition to traditional absorption contrast tomography, several other contrast mechanisms have recently begun to be employed. One is phase contrast, which is based on the difference in the X-ray phase (real part of the complex X-ray refractive index) between two materials. Phase contrast varies much more slowly with X-ray energy than absorption (the imaginary part of the X-ray refractive index). Phase contrast also varies more slowly with atomic number than absorption, so even low-Z elements such as carbon have significant phase contrast at high X-ray energies. Phase contrast is thus an excellent technique for looking at interfaces in low-Z materials, such as in plants and the soft tissue of animals. Another contrast mechanism is X-ray fluorescence, which provides trace element sensitivity, but has a number of constraints on collection time and sample size which are discussed below. Finally, contrast based on X-ray powder diffraction can be used to image the distribution of crystalline phases.

1.2. Microtomography

The spatial resolution of the medical scanners is not sufficient for many problems in materials science, biology, and Earth science, where resolutions in the micron range or below are required for many problems. This has led to the development of computed microtomography systems with significantly better spatial resolution and smaller fields of view. These have developed in three 'generations', largely due to improvements in X-ray detectors (Figure 1).

First-generation tomography employs a pencil beam and a detector with no spatial resolution. Such detectors include ion chambers, photomultiplier tubes, and photodiodes. In first-generation tomography the sample must be translated into number-of-pixels steps across the beam to measure the line-integral of each ray at one angle. The sample is then rotated by a small amount ($180°$/number-of-angles), and the translation scan performed again. The data for a single slice requires number-of-pixels $*$ number-of-angles moves and measurements, and is thus quite slow. Collecting multiple slices to construct a 3-D dataset requires movement of the sample vertically, and repeating the translate/rotation operations. One advantage of this method is that the X-ray beam can be collimated tightly just in front of the detector to eliminate
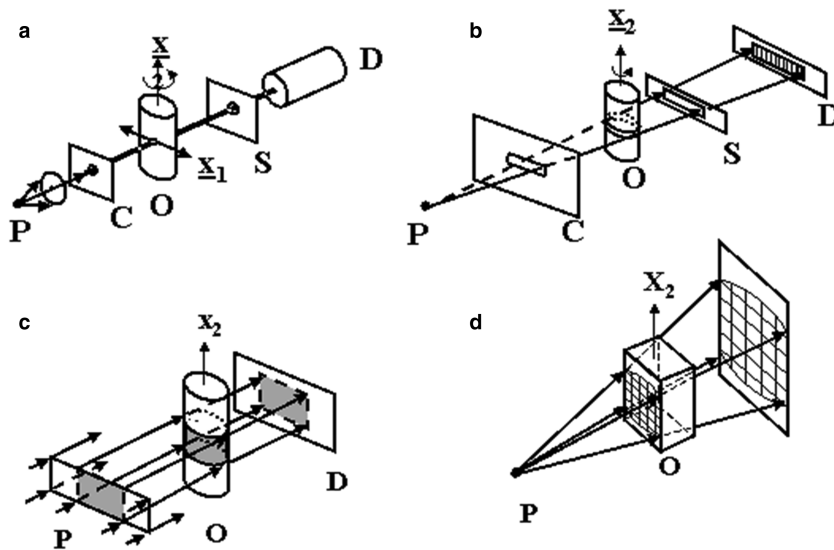
Figure 1. Experimental approaches for X-ray computed tomography. P = primary beam, C = collimator, O = object, S = slit, D = detector. (a) First Generation using a pencil beam. Sample is translated and rotated to collect a single slice. (b) Second Generation using a fan beam. Sample is rotated to collect a single slice. (c) Third generation using a parallel beam such as from a synchrotron. Sample is rotated to collect multiple slices. (d) Third generation using a cone beam from an X-ray tube. Sample is rotated to collect multiple slices.

scattered X-rays from the sample. This leads to greater data quality compared to 2-D detectors used in third-generation tomography, where collimation is very difficult, particularly with small pixel sizes.

Second-generation tomography uses a fan beam and a 1-D detector. It can thus measure all of the projections for a single slice of the sample at a single angle simultaneously. This speeds up the data collection, as now the sample only needs to be moved for each angle, but not for each pixel. It is still possible to collimate the transmitted beam in front of the detector in the vertical direction, again to reduce the scatter signal. A 3-D data set requires number-of-angles ∗ number-of-slices moves and measurements, so this setup is still rather slow.

Third-generation tomography uses either a large parallel beam from a synchrotron or a cone beam from an X-ray tube, and a 2-D detector. This technique is much faster, as a complete 3-D dataset requires only number-of-angles rotations of the sample and no translations. The technique typically does not have ability to shield against scattered X-rays, which can reduce the image quality.

The field of microtomography has advanced rapidly in the last 15 years due to the introduction of third-generation tomography systems. These developments have been made possible due to advances in X-ray sources, detectors, and computer systems.

1.3. Laboratory X-ray sources

X-ray microtomography systems can be laboratory-based or synchrotron-based. Laboratory-based systems use X-ray tubes as the source. These tubes can be optimized for high spatial resolution, and employ micro-focus electron beam spots, relatively low accelerating voltage (<100 kV) and relatively low tube current (<10 mA). Such sources are well suited to small low-Z samples to be imaged at high resolution. For imaging large samples, tubes operating at high voltages (>200 kV) and higher currents are used, because the electron beam spot can be larger. Regardless of tube type, laboratory sources are polychromatic; the X-rays include the characteristic emission lines of the tube anode (Cu, Mo, W, *etc.*) and also the broadband *bremsstrahlung* radiation. Tube sources emit X-rays in all directions, and laboratory tomography system collect a significant angular range in both second-generation fan-beam and third-generation cone-beam geometries (Figure 1). Because they have a diverging X-ray beam, laboratory sources have X-ray magnification determined by the ratio of the distances from the source to the sample and from the source to the detector. Because laboratory systems utilize a broad energy range and a significant angular range they are more competitive with synchrotron systems than the brightness ratio of the sources (10^6 or more) would suggest. However, laboratory systems are subject to several artifacts. The first is due to the fact that when using polychromatic radiation, the value of μ in equation 1 is not well defined. Each X-ray energy passing through the sample has a different μ value. The lower-energy X-rays are absorbed more rapidly in passing through the sample than the high-energy X-rays. This leads to beam-hardening artifacts, which cause a uniform object to appear to be less absorbing (lower μ) in the interior than on the edges. These artifacts can make it difficult to segment the images because regions of the same material appear to have different μ values depending on their location in the sample. Beam hardening artifacts can be reduced by pre-hardening the beam with absorbers during data collection, or by software corrections during data processing. The second type of artifact arises when the cone-beam angle is large. It is not possible to do an exact tomographic reconstruction in this case, and geometric artifacts occur.

1.4. Synchrotron X-ray sources

Synchrotron radiation is an excellent source for microtomography systems (Kinney and Nichols, 1992; Sutton *et al.*, 2002). The details of synchrotron radiation are covered in the chapter by Waychunas (2014, this volume). Bending magnet and wiggler sources provide relatively large beams, up to 100 mm wide or more, and typically 3–8 mm high at the sample position, depending on the energy of the storage ring, the X-ray energy, and the distance of the sample from the source. These sources are inherently broad bandwidth, but they are sufficiently intense that monochromators can be installed to select a small-energy bandwidth. High-resolution crystal monochromators, such as Si (111) with bandwidths of $\sim10^{-4}$ can be used. Multilayer monochromators provide much larger bandwidths ($\sim10^{-2}$) and thus greater flux, though typically at the expense of a lower high-energy limit than crystal monochromators. Because

synchrotron microtomography is generally performed with such monochromatic X-ray beams it is not subject to the beam hardening artifacts of laboratory systems.

Because the source is far from the sample, typically 20–60 m, and the sample is relatively small, typically 10 mm or less, the X-ray divergence angle on the sample is very small. For example with a 10 mm sample 50 m from the source, the range of angles on the sample is only 0.2 mrad. This means that if the sample width covers 1000 pixels on a detector, the divergence is only 0.2 pixels, and the beam can be considered to be parallel for practical purposes. The parallel beam geometry greatly simplifies tomographic reconstruction, and eliminates the cone-beam artifacts described above. The parallel beam does, however, require that the detector system have small pixels, because there is no X-ray magnification unlike laboratory tube-based systems.

Synchrotron undulator sources produce much more intense X-ray beams that are highly collimated in both the horizontal and vertical directions. Typical beam sizes at the sample position 50 m from the source is 2 mm horizontally and 1 mm vertically. Undulators are thus excellent sources for imaging small samples, while bending magnets and wigglers are better for larger samples.

It is also possible to use the beam from a bending magnet, wiggler, or undulator without a monochromator. This is called 'white beam' imaging if there is no X-ray mirror in the path, or 'pink beam' if the X-rays are first reflected from a mirror. With white or pink beam the flux is increased by a factor of 10^2–10^4. This allows very high-speed imaging, with time resolution down to the 100 ps single-bunch time of the storage ring, but more commonly in the millisecond range. White beam, typically filtered with absorbers to remove low-energy X-rays, is often used for high-energy tomography at beamlines where the high-energy flux is too low to use a monochromatic beam. Of course when using white or pink beams the beam hardening artifacts described above for tube sources can also be a problem.

Both laboratory and synchrotron sources have advanced significantly in the last 15 years. Laboratory sources are now available with much smaller X-ray source diameters, which greatly reduces penumbral blurring in imaging applications. Synchrotron sources have increased in energy with 6–8 GeV sources, and greatly increased in brightness with the development of very low-emittance storage rings and undulator sources.

1.5. Detectors

Third-generation microtomography is possible due to the rapid recent advances in 2-D charge-coupled device (CCD) and complementary metal-oxide semiconductor (CMOS) detectors. Such detectors were not available before ∼20 years ago, and they have improved rapidly. Detectors with 5 million pixels or more that can be read out at up to 100 frames/s are now available. CCD detectors and new scientific CMOS detectors have very low read noise (<10 electrons). For tomography applications the transmission is typically at least 10% and the noise is most often limited by the Poisson statistics rather than the read noise of the detector. The Poisson is limited by the number of electrons in the full-well of the detector (Rivers *et al.*, 2010).

The 2-D semiconductor detectors (CCD and CMOS) are generally not well suited for direct detection of X-rays. This is both because the Si is too thin (<300 μm) to efficiently detect the X-rays, and also because a single X-ray produces thousands of electrons, which will fill up the full well capacity of a pixel with fewer than 100 X-rays. Instead of directly illuminating the CCD the X-ray are first converted to visible light with a scintillator. For high-resolution tomography thin single-crystal scintillators made of yttrium aluminum garnet (YAG), lutetium aluminum garnet (LuAG), CsI, or $CdWO_4$ are commonly used. The visible light is then imaged onto the CCD detector using lens or fiber-optic coupling. By using interchangeable lenses the system is more flexible, because the magnification and hence field of view and resolution can be changed easily. The thickness of the scintillator involves a trade-off between efficiency and spatial resolution, and this is a function of X-ray energy. Thicker scintillators absorb a larger fraction of the X-rays, but at the expense of resolution due primarily to the depth of focus effect, but also X-ray and visible light scatter. Scintillators of $100-250$ μm are commonly used for spatial resolutions of a few microns, but for sub-micron resolution, thinner scintillators must be used.

1.6. Computers

Computed tomography is very data intensive, and is always pushing the limits of computer technology. For example, in 1987 the time to collect a single 512×512 pixel tomographic slice using first-generation CT was ~1 h, and it also took ~1 h to reconstruct that slice on a MicroVAX workstation (Spanne and Rivers, 1987). A single slice would have required ~1% of the storage of a state-of-the-art 600 MB disk at that time. Today a $2048 \times 2048 \times 2048$ voxel dataset can be collected in a few minutes with a CCD detector and the entire dataset can be reconstructed in <2 min on a single 8-core workstation (Rivers, 2012). Such a dataset requires 32 GB on disk, which is ~3% of a current 1 TB hard disk. It requires a workstation with 24 GB of random access memory or more. The improvements since 1987 are close to a factor of a million, and current computed tomography would be impossible without these gains.

2. Absorption Tomography

The following section describes important aspects of how absorption tomography is performed, including parameter optimization, data collection, data reconstruction, and data analysis.

2.1. X-ray energy and sample size

X-ray absorption is a strong function of the sample composition and X-ray energy. It is thus essential to select the X-ray energy to match the sample size and composition. The characteristic absorption depth, *i.e.* the depth at which the transmission is $1/e$ or 36.8% for some common minerals is shown in Figure 2. The energy to achieve this transmission through 1 mm of quartz is ~18 keV. The same thickness of calcite requires
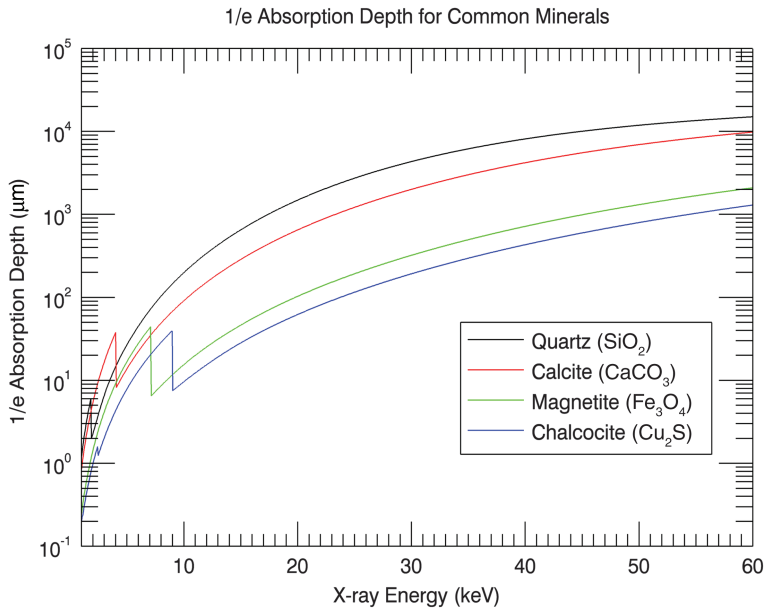
Figure 2. The characteristic (1/e) absorption depth for some common minerals as a function of X-ray energy.

24 keV, while magnetite and chalcocite require 45 and 55 keV respectively. The optimum sample thickness results in transmission between $\sim e^{-1}$ and e^{-2}, or 14% to 37%. This is a tradeoff between having sufficient absorption to be able to detect it from the noise in the counting statistics, and not too much absorption so there are sufficient X-rays transmitted to be able to measure with good statistics. The maximum absorption along a ray is what is important. At 20 keV, for example, magnetite has a 1/e depth of ~ 25 μm. This means that if two 50 μm crystals of magnetite are located in the same slice, then there will be some rays that will have to pass through 100 μm of magnetite, and the transmission will be only $e^{-4} = 1.8\%$. The absorption is so large that the measurement will be subject to large uncertainty, and may lead to artifacts in the reconstruction. There will be an upper limit to the size of the sample that can be imaged on a given instrument based on the X-ray energies available and the sample composition.

2.2. Data collection

A schematic of a third-generation setup at a synchrotron is shown in Figure 3. Data collection for third-generation absorption tomography consists of taking a series of 2-D projections or radiographs at small angular steps as the sample is rotated from 0 to 180°. The minimum angular step size can be calculated as follows:

– The detector has N pixels in the direction perpendicular to the rotation axis, each pixel is size P, so the detector width is NP.
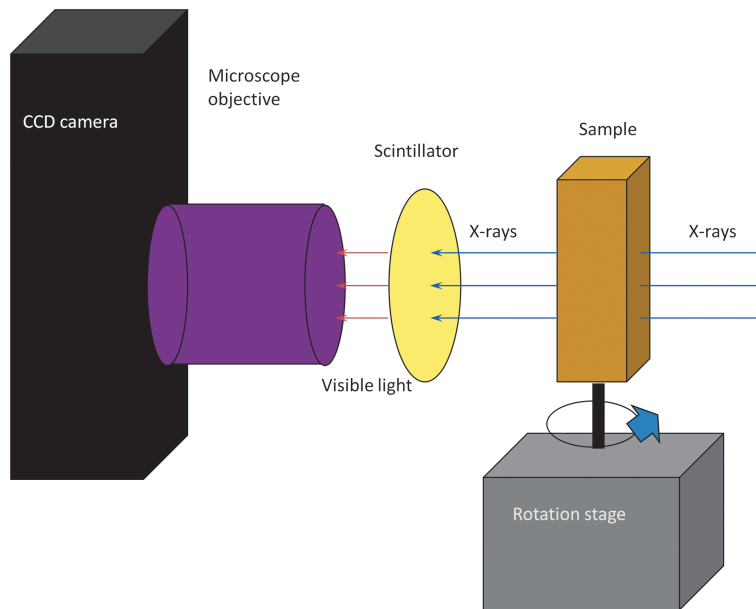
Figure 3. Schematic of a typical setup for third-generation tomography at a synchrotron. A parallel beam of monochromatic X-rays enters from the right and passes through the sample and is partially absorbed. The X-rays then strike a scintillator crystal which converts the X-rays into visible light, which is then imaged with a lens and CCD camera. Data collection consists of rotating the sample over $180°$ and collecting images at fine angular steps, *e.g.* every $0.2°$.

–   Consider a sample that fills exactly the field of view of the detector, so the sample diameter is also *NP* and its radius $R = NP/2$.
–   Consider a point on the sample that is in the center of the field of view on the upstream or downstream periphery of the sample, so its distance from the rotation axis is $NP/2$.
–   What is the angle that moves that point on the sample by exactly 1 pixel?

   The solution is that the angle step $θ = P/R = 2/N$. The number of angles to cover $180°$ ($π$) is $πN/2$. Thus, if the rotation axis is vertical and the detector has 1024 pixels in the horizontal direction one should collect 1608 angles. In practice, fewer than $πN/2$ angles are collected in many cases, to reduce measurement time, but if the number of angles is too small it will lead to aliasing and artifacts. Improved image quality can be obtained by collecting more than the required number of angles because of simple signal to noise considerations: more measurements reduces statistical noise, typically as the square root of the number of X-rays collected.

   Several important mechanical alignment requirements are involved when collecting   **Q1** tomography data. For the third-generation parallel beam geometry (Figure 1c) these are: (1) the rotation axis must be perpendicular to the X-ray beam propagation direction;

and (2) the rotation axis must be parallel to the columns of the 2-D detector. If these alignments are correct then, as the sample is rotated, each row of the detector collects data from the same slice perpendicular to the rotation axis. Conversely, if these alignments are not correct then each detector row contains information from multiple slices, and image artifacts will result.

2.3. Data normalization

In addition to the projections of the sample (PJ) it is necessary to obtain data for the dark current (DC) and the flat field (FF). The dark current is the signal measured in the detector when the X-ray beam is turned off. The flat field is the signal in the detector with the sample completely removed from the X-ray beam. The projections are normalized as follows

$$\text{PJ}_{\text{normalized}} = (\text{PJ}_{\text{raw}} - DC)/(FF - DC) \qquad (2)$$

Each pixel in the normalized projection thus represents I/I_0, the transmitted intensity divided by the incident intensity. This is the line integral of the absorption along that ray through the sample. If the detector is $1\,K \times 1\,K$ pixels and 1000 projections are collected there are >1 billion measurements of I/I_0!

The above steps are shown in Figures 4–6 for an example data set of a soil aggregate. This was imaged on the 13-BM-D beamline at the Advanced Photon Source at Argonne National Laboratory. The measurement parameters are shown in Table 1.

A total of 900 raw projections was collected as the sample was rotated over 180° (Figure 4). The dark current for this detector is a uniform 100 counts in every pixel when there are no X-rays, independent of exposure time. This value was thus subtracted from all pixels in the raw projections and flat field images. A total of 50 flat field images (Figure 5) was collected during the experiment: 10 at the start of the experiment, 10 every 55.2°, and 10 at the end. The flat field image has several features of interest. The intensity is greatest in the vertical center of the field of view, and decreases at the top and bottom. This is due to the pseudo-Gaussian intensity distribution from the synchrotron bending magnet source. The dark
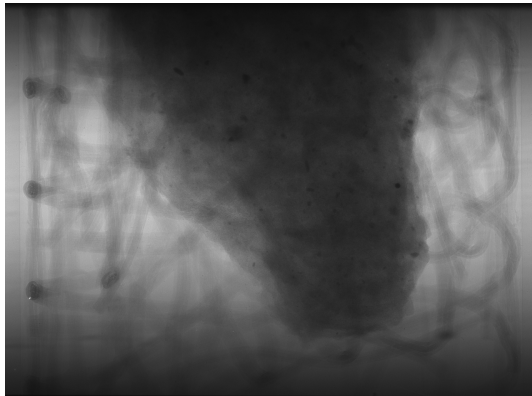

Figure 4. Raw projection of a soil aggregate sample at 0° rotation angle. 900 such projections were collected at an angular increment of 0.2°. For this measurement the field of view did not extend to air on each side of the sample, but rather the left and right edges of the image are the plastic tube containing the sample. The sample was held in place in the tube with glass wool. The gray-scale in this image covers the entire 0–4095 count range of the CCD detector.
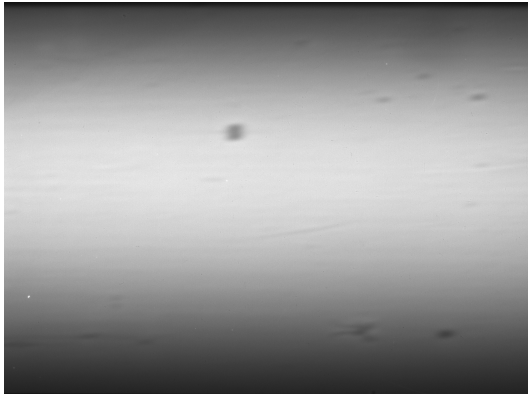
Figure 5. Flat-field image collected with the sample in Figure 4 removed from the beam. A total of 50 such images were collected. The gray-scale in this image covers the entire 0–4095 count range of the CCD detector.

blurry spots are due to imperfections in the Si (111) crystals of the monochromator, which cause the diffracted beam intensity to be low. They are not sharp because they are ~25 m upstream of the scintillator, and the finite size of the electron beam source causes penumbral blurring. The bright sharp spots are caused by dust on the scintillator which allow extra light from the scintillator to escape due to refractive index effects. Note that the intensity in the flat fields should not be too low in any region to avoid noise due to poor statistics. Equally important is that the flat-field intensity be stable with time, or else the estimate of I_0 in each pixel will be incorrect. This is of course a function of the stability of the storage ring and the beamline optics. The flat field images were all averaged together to produce a low-noise measurement of the incident beam profile. All 900 projections were then divided by this averaged flat field to produce normalized images (Figure 7). The normalized images have uniform intensity in the air and plastic, and the monochromator and scintillator imperfections are no longer visible.
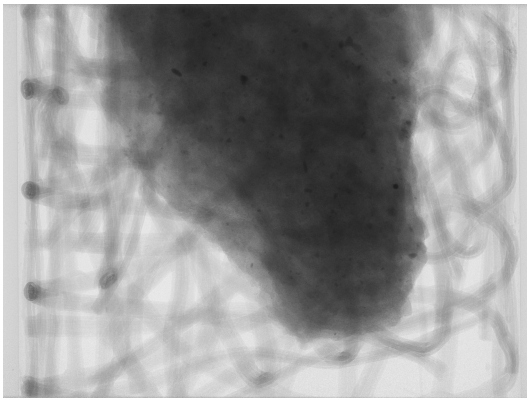

Figure 6. Normalized projection of a soil aggregate sample at $0°$ rotation angle, which is the image in Figure 4 corrected for dark current and normalized to the average of the 50 flat fields such as that shown in Figure 5. The gray-scale in this image covers the range from 0 to 100% transmission.

2.4. Sinograms

The next step in the data processing is to construct the sinogram from the data for a single slice perpendicular to the rotation axis. These are the data for a single row of the CCD detector as a function of rotation angle (Figures 7–9). The normalized data for the center row of the detector (519) are shown in Figure 7. This is an X-θ slice of the dataset, where the horizontal direction is one row of the CCD (and thus the X position on the sample) and the vertical direction is the rotation angle θ. Note that in this view all

Table 1. Experimental parameters for a sample soil-aggregate data set.

Exposure time	0.65 s
Image size	1392 pixels × 1040 pixels
Pixel size on sample	6.51 μm × 6.51 μm
Field of view	9.06 mm × 6.77 mm
X-ray energy	28 keV
Number of projections	900
Angle between projections	0.2°
Flat field measurements	50
Total collection time	14 min

objects in the sample will describe one half cycle of a sin wave as the sample is rotated over 180°, hence the term sinogram. The sinogram must next be converted to a logarithmic scale, so that the value of each pixel is $-\log(I/I_0)$. This operation is necessary for absorption data because absorption is exponential with thickness. The quantity that is conserved in absorption data is the sum of $-\log(I/I_0)$ for all rays through the sample, regardless of sample rotation angle. On the other hand the signal for fluorescence is linear with thickness, and so the logarithm is not done when processing fluorescence tomography data. The same row is shown in Figure 8 as in Figure 7, but after taking Figure 8. The areas of low absorption are close to 0, and the brightest regions of the image have a value of ∼1.5. The final step in producing the sinogram is to apply a high-pass filter. This is necessary to produce accurate reconstructions with the filtered back-projection and related methods, as illustrated in the next section. The same row is shown in Figure 9 as in Figures 7 and 8, but after removing the low-frequency components of the sinogram with a high-pass Shepp-Logan filter.

2.5. Reconstruction

The key transformation in tomography is reconstructing a cross section of the object from the sinogram. The most common reconstruction method, and probably the easiest to understand, is filtered back-projection. This method can be described using the following steps. First, create an $N \times N$ array with all 0 values, where N is the number of pixels in the horizontal direction in the sinogram, *i.e.* the number of columns in the detector.

For each row of the sonogram, sum the projection of that row with the current contents of the array. The projection is done at the angle at which that row of the sinogram was collected. One can think of projection as creating a mask where the transparency of
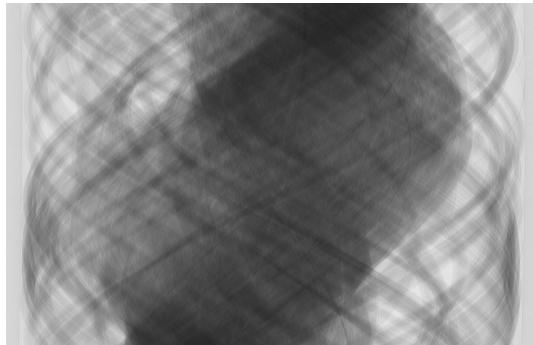

Figure 7. Normalized data for row 519 of the CCD detector. In this image the horizontal direction is the column of the CCD detector (X position on sample) and the vertical direction is the rotation angle θ.
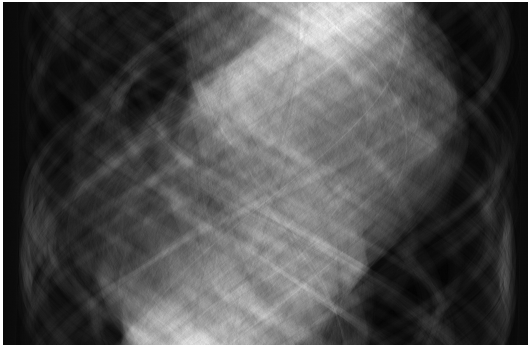
Figure 8. Normalized data for row 519 after converting to $-\log(I/I_0)$.

the mask is proportional to the value of the sinogram in that pixel, and then shining a parallel light source through the mask across the array. As each row of the sinogram is back-projected the image accumulates, until a complete image is formed after $180°$. The process is illustrated in Figure 10. Only the first row of the sinogram (at $0°$) has been back-projected in Figure 10a, so there are just horizontal stripes of various intensities in the image. All 25 projections from $0°$ to $5°$ have been summed in the Figure 10b. Similarly, the summations of projections from $0°$ to $45°$, $90°$, $135°$, and $180°$ are shown in Figures 10c to 10f, respectively. The reconstruction clearly contains artifacts that are reduced as the angular range of the projections increases, until finally at $180°$ an accurate cross section is produced.

Because filtered back-projection involves a summation of the values in each sonogram, the need for filtering the sinograms first is obvious. As each value in the sinogram is $-\log(I/I_0)$, and as I will be $<I_0$, the values in the sinogram will always be positive. Thus when they are back-projected (summed) the total intensity continues to grow larger with the number of angles, and there will never be any zero values in the reconstructed image. But all areas with no sample should have zero in the reconstruction. Clearly what is needed is to have some of the sinogram values negative so that the sum can be zero where it should be. This is accomplished by applying a filter that effectively takes the derivative of the sinogram, producing both positive and negative values. The effect of using no filter when reconstructing, com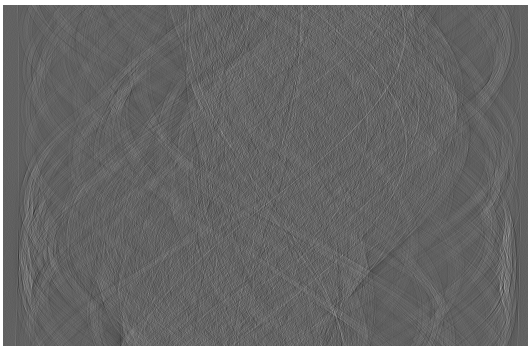pared to using a Shepp-Logan filter, is shown in Figures 11 and 12. In the reconstruction with no filter (Figure 11) the object is recognizable, but the reconstruction has a large intensity 'dome' in the center of the image. The reconstruction with the Shepp-Logan filter (Figure 12) reproduces accurately the linear attenuation values in the sample.

There is one parameter that must be optimized when performing the reconstruction. This is the location of the pixel that contains the rotation axis. Generally the rotation axis will be aligned near the
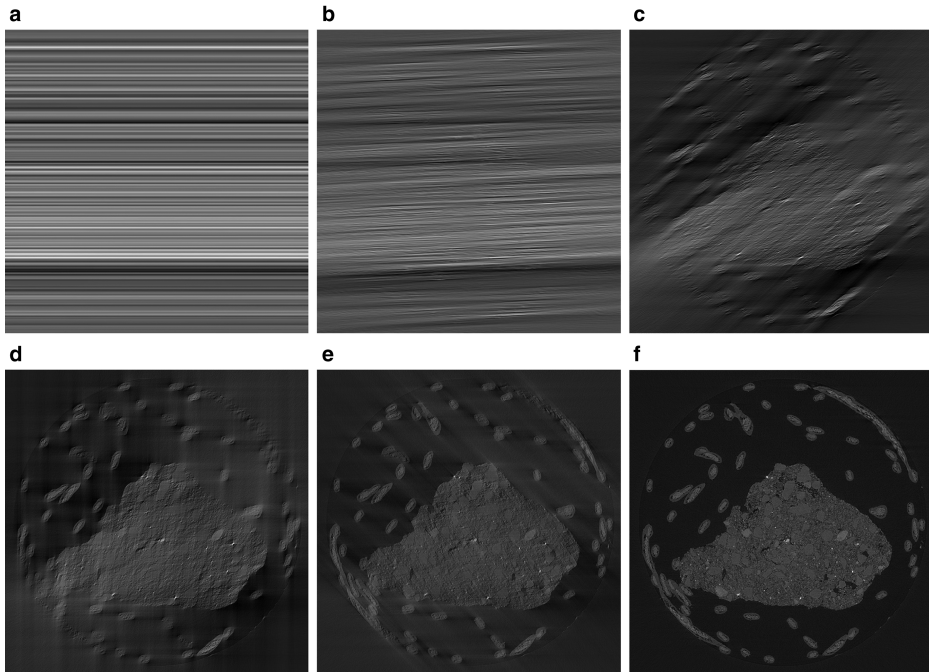

Figure 9. Normalized data for row 519 after converting to $-\log(I/I_0)$ and filtering with a Shepp-Logan filter.

Figure 10. Reconstructions using filtered back-projection over different angular projection ranges. (a) 1 projection at $0°$. (b) 25 projections from $0–5°$. (c) 225 projections from $0–45°$. (d) 450 projections from $0–90°$. (e) 675 projections from $0–135°$. (f) 900 projections from $0–180°$.

center of the images when data are collected. When reconstructing however, the exact location of the rotation axis must be determined, preferably to sub-pixel accuracy, or artifacts will result. The reconstruction of slice 519 shown in Figure 12 was done with the rotation axis at pixel 694.5. The reconstruction with the rotation axis two pixels to the left, at pixel 692.5 is shown in Figure 13. The bright mineral grains in the sample have a crescent shape, with the crescents opening to the left. The reconstruction with the rotation axis two pixels to the right, at 696.5 is shown in Figure 14. The bright mineral grains are again crescent shaped, but now the crescents open to the right. The pixel containing the rotation axis can be optimized manually by visually minimizing such artifacts though It is more convenient and accurate to use an automated method for optimizing the rotation axis. A plot of the image entropy for reconstructions of a slice near the top of this sample (104) and another near the bottom (700) as a function of the rotation axis position is shown in Figure 15. The image entropy is a measure of the sharpness of the intensity histogram of each image and is computed as

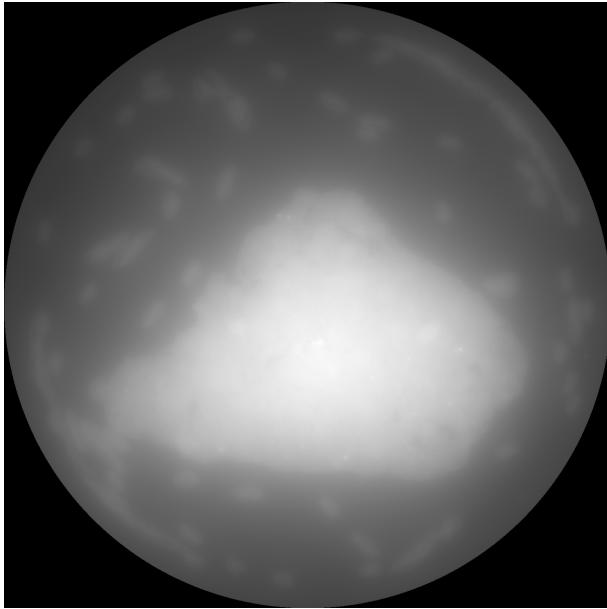$$\text{entropy} = \sum_{i=0}^{N} H_i \log(H_i) \tag{3}$$

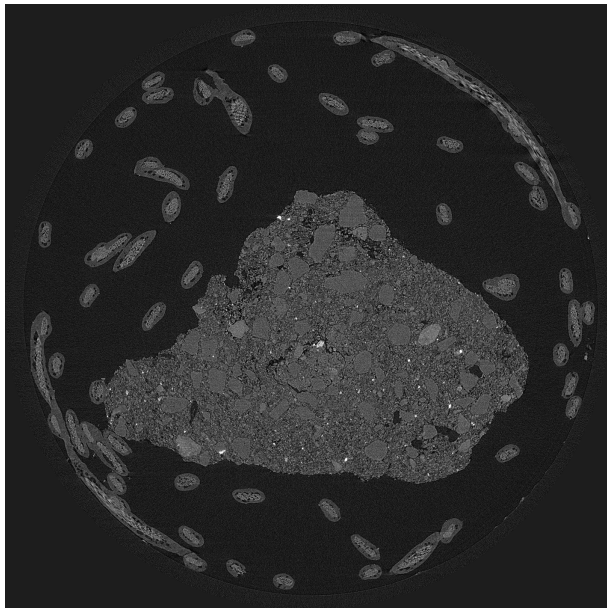**Figure 11.** Reconstruction without filtering the sinogram.

Figure 12. Reconstruction with the sinogram first filtered with a Shepp-Logan filter.

where N is the number of elements in the histogram, and H_i is element i of the histogram. The optimum rotation axis position can clearly be found to 0.25 pixel accuracy with this technique. If the system were perfectly aligned the rotation axis would be in the same pixel for the slice at the top of the sample and the slice at the bottom of the sample. In this case the rotation axis is 0.5 pixels larger for slice 104 than for slice 700, so the rotation axis is not perfectly parallel to the columns of the CCD.

Once the rotation center position is determined, the final step is to reconstruct all of the slices in the data set, *i.e.* the number of rows in the projections. This has traditionally been a very time-consuming step, and large computing clusters have been used to distribute the reconstruction of the slices. However, modern multi-core workstations are now capable of reconstructing large datasets in a very reasonable time (Rivers, 2012). For example, the dataset used for illustration here is $1392 \times 1040 \times 900$ (X, Y, Projections) which is reconstructed to a $1392 \times 1392 \times 1040$ (X, Y, Z) volume. This was reconstructed in 35 s on a modern

8-core Windows® workstation. The 3-D reconstructed volume can be visualized with 2-D slices (Figures 16, 17) in any direction, by movies flying through the object, or by volume rendering.

2.6. Spatial resolution

The spatial resolution in absorption tomography is controlled by the following factors.

2.6.1. Source size. The X-ray source has a finite size, either the size of the electron beam spot on the anode in an X-ray tube, or the size of the electron beam in the storage ring for synchrotron radiation. This source size limits the spatial resolution that can be achieved on the detector because of the finite distance of the sample to the detector. For example, at the Advanced Photon Source (APS) bending magnet the full-width at half maximum (FWHM) of the electron beam in the horizontal direction is ∼250 μm. This distance from the source to the sample is ∼50 m and the distance from the sample to the scintillator might be 0.1 m. X-rays from the source passing through a point in the sample will thus form a 50/0.1
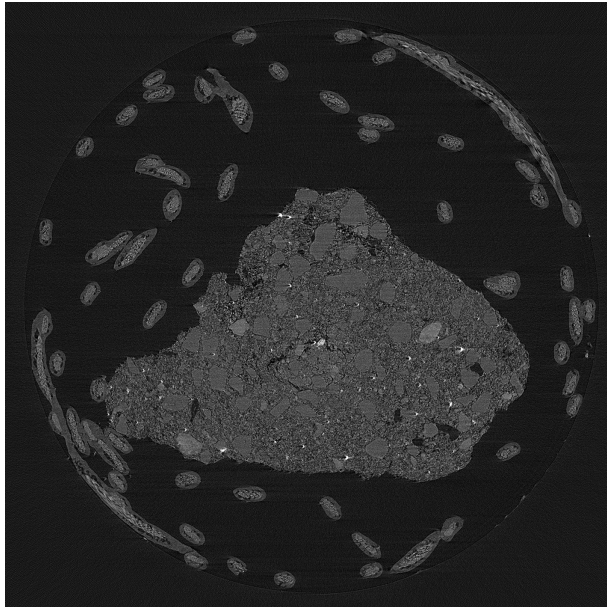

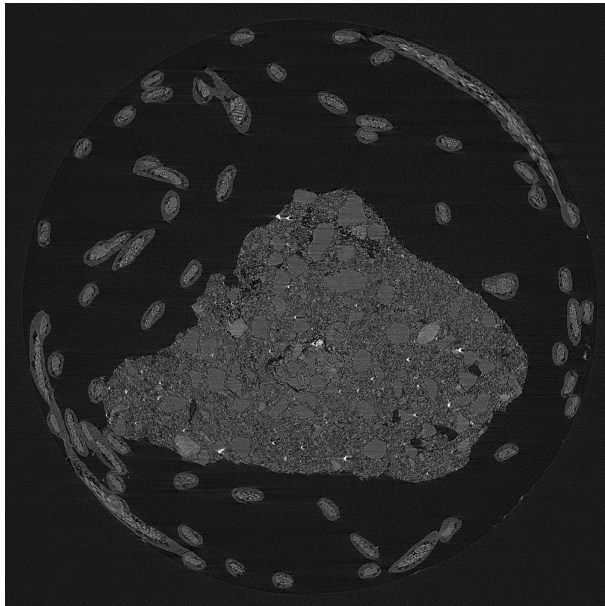**Figure 13.** Reconstruction with the rotation center −2 pixels from the optimum value.

Figure 14. Reconstruction with the rotation center +2 pixels from the optimum value.
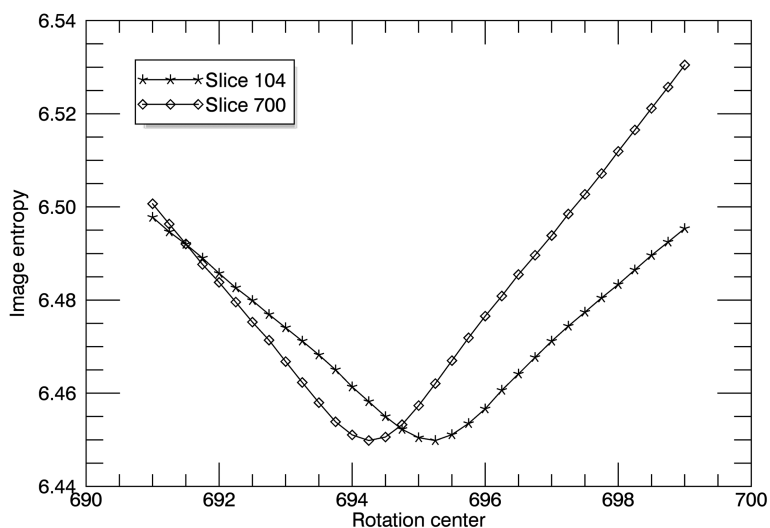
Figure 15. Image entropy in reconstructions of slices 104 and 700 as a function of the rotation center position.

(= 500) times demagnified image of the source on the scintillator. A point on the sample will thus be blurred by 250 μm/500 = 0.5 μm on the scintillator. This is thus one limit on the spatial resolution that can be obtained. Larger source sizes or larger sample to scintillator distances will of course increase this value.
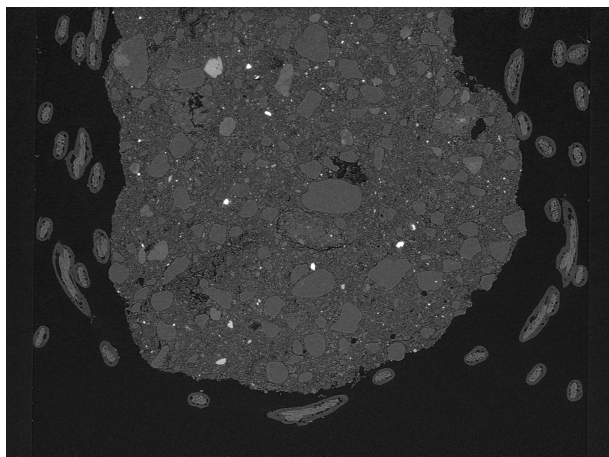

Figure 16. Slice 869 through the reconstruction of the soil aggregate in the vertical direction parallel to the X-ray beam.

2.6.2. Sample and detector size. Tomography is generally performed with the sample entirely in the field of view. The spatial resolution is then limited by the size of the sample and the number of pixels in the detector. For example if the sample is 9 mm in diameter and is imaged with a field of view of 10 mm (with 0.5 mm of air on both sides), and the detector has 2000 pixels horizontally, then the pixel size

will be 5 μm. In order to have each pixel on the detector correspond to 1 μm in the sample, the field of view and hence sample size, would need to be restricted to 2 mm.

Figure 17. Slice 779 through the reconstruction of the soil aggregate in the vertical direction perpendicular to the X-ray beam.

2.6.3. Visible-light diffraction limit.

Most microtomography detector systems first convert the X-rays to visible light, and then image this light with lenses onto the detector. A fundamental limit on spatial resolution comes from the diffraction limit of visible light, which is

$$d = \lambda/(2NA) \tag{4}$$

where d is the diffraction limited resolution, λ is the visible light wavelength, and NA is the numerical aperture of the lens. λ is ~ 0.5 μm for the visible light from most scintillators. The NA of the lenses typically used in tomography systems which require relatively long working istances are $0.1–0.5$ depending on magnification. This leads to diffraction-limited resolutions of $0.5–2.5$ μm.

2.6.4. Scintillator limits.

There are a number of spatial-resolution limits that arise from the scintillator itself. One is the depth of focus from the finite thickness of the scintillator required to efficiently stop the X-rays. A second is light scattering and light leakage that arises because the scintillators are all high atomic number materials with large refractive indices. This leads to complete internal reflection for light emitted at angles less than a rather large critical angle. Finally as X-rays are stopped in the scintillator they generate secondary electrons and fluorescent X-rays that travel a significant distance before they stop and generate light.

2.6.5. Rotation stage limits.

Most rotation stages have wobble of at least 1 μm. Some air-bearing stages reduce this to a few tenths of a micrometer.

For all of the above reasons the true minimum spatial resolution in most microtomography systems is about 1 μm, even if the data are collected with pixels that are smaller than this.
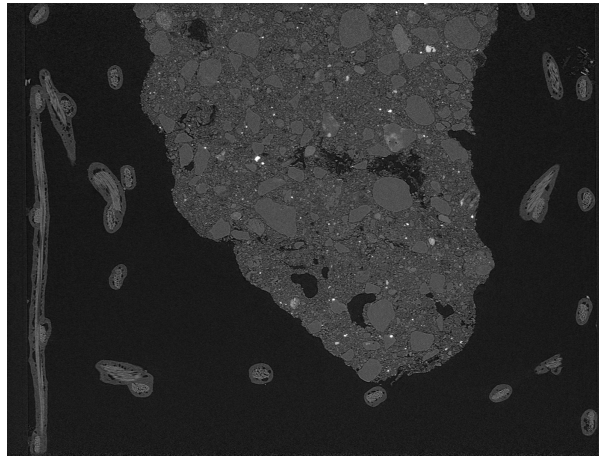
2.7. Contrast resolution

The values at each voxel in the reconstructed data are the X-ray linear attenuation coefficient (μ) at the energy of the measurement. The differences in μ for each material in the sample are what generate the contrast in the images. Minimizing the noise in the measured μ values is important for image analysis. If the noise is large then the μ values of different phases will overlap, making image segmentation difficult.

For the CCD cameras used for microtomography the minimum noise in the measurement at each pixel is controlled by the CCD pixel full-well capacity in electrons. This is typically $\sim$16,000 electrons. The noise is controlled by Poisson statistics on this number, so the expected percent noise is $100 * \dfrac{\sqrt{16000}}{16000} = 0.79\%$. This is very close to the measured statistical noise in the detector in use at 13-BM-D at the APS. The noise in the images after normalization is similar, 0.82%. But the noise in a uniform area of a reconstructed image increases by a factor of $\sim$6–4.7% (Rivers *et al.*, 2010). This increase in noise is inherent in the reconstruction process because of the high-pass filter that is required before back-projection. The filter essentially takes the derivative of the measured data, which increases the noise. The 4.7% noise in the reconstructed values means that it will be difficult to segment materials that differ by $\sim$10% or less in μ.

3. Differential Absorption Tomography

The energy 'tunability' of synchrotron X-rays sources makes possible the technique of differential absorption tomography. In this method tomography datasets are collected just above and just below an X-ray absorption edge of an element of interest. The main requirement of the method is that the sample must have sufficient X-ray transmission at the X-ray edge energy. For soil or rock samples that are greater than a few mm in size only absorption edges $>\sim$20 keV can be used. This precludes measurements of the first-row transition elements (Mn, Fe, Zn, *etc.*) For example it can be seen from Figure 2 that the $1/e$ absorption depth for quartz at the Fe absorption edge (7.11 keV) is only $\sim$50 μm, so this energy will not be transmitted through more than $\sim$150 μm of quartz. However, the technique has found wide application using elements such as Cs and I as contrast agents for imaging fluids in porous media (Wildenschild *et al.*, 2013). The X-ray linear absorption coefficients for quartz, water, and water with 1 mol.% CsCl or KI are shown in Figure 18. Below the absorption edge, quartz is more absorbing than the fluid, but above the absorption edge fluid is more absorbing than quartz. This dramatic change in contrast of the fluid can be used to construct difference images (Figure 19). The fluids (Figure 19a) are very difficult to see and have such similar absorptions they would be impossible to distinguish from each other, and both absorptions are so small that they are difficult to distinguish from air. Above the I absorption edge (Figure 19b) however, the organic fluid becomes strongly absorbing, but is now quite similar to quartz. Above the Cs absorption edge (Figure 19c) the aqueous phase is also strongly absorbing, and is again impossible to distinguish from the organic fluid. However, by subtracting images b–a (Figure 19d) the organic
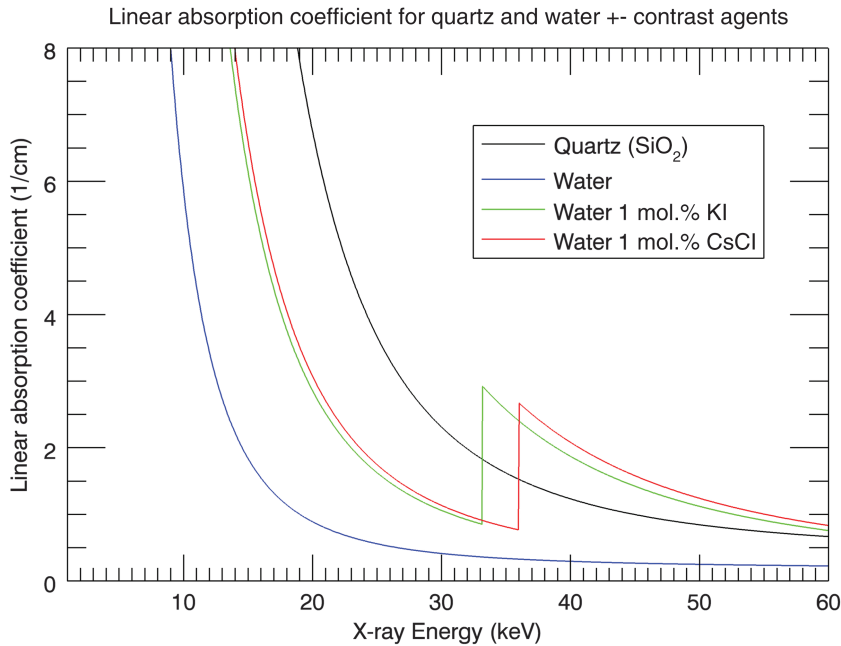
Linear absorption coefficient for quartz and water +- contrast agents

Figure 18. The X-ray linear absorption coefficient (cm^{-1}) for quartz, water, and water with 1 mol.% CsCl or KI over the energy range from 0 to 60 keV. The I K absorption edge is at 33.169 keV and the Cs K absorption edge is at 35.985 keV.

Q2

fluid containing I is the only bright phase in the difference image. Similarly by subtracting images c−b (Figure 19e) the aqueous phase containing Cs is the only bright phase in the difference image. Interestingly these images show that in this exper-iment it is the organic fluid that is wetting the glass beads (Figure 19d), and the aqueous phase is non-wetting. This is because the glass beads were coated with a hydrophobic material.

4. Phase-Constrast Tomography

Absorption tomography discussed above is based on contrast due to X-ray absorption, which arises from the imaginary part of the complex X-ray refractive index. Absorption contrast varies strongly with atomic number and with X-ray energy. Phase-contrast imaging is based on the real part of the refractive index, and varies more slowly with X-ray energy and atomic number. There are a number of techniques available to image phase contrast, including in-line image propagation (Mayo *et al.*, 2012), Talbot interferometry (Weitkamp *et al.*, 2005), analyzer crystals for diffraction-enhanced imaging (Chapman *et al.*, 1997), and holography (Momose *et al.*, 1996). The simplest technique to implement is in-line image propagation, which involves simply increasing

the distance between the sample and the detector. X-rays are bent (refracted) at interfaces between materials with different real-parts of their refractive index. This small angle becomes a measureable displacement as the sample-to-detector distance increases. The phase contrast is a function of the coherence of the X-ray source, which makes synchrotron sources very useful. Because even low-Z elements such as carbon have a substantial phase contrast, this technique is potentially very useful for imaging the interfaces of organic matter in soils. Phase-contrast imaging can also be useful to visualize very small features close to the resolution of the setup used. An interesting application was using phase contrast to study reactions in mortar (Marinoni *et al.*, 2009)

Reconstructed cross sections of a rhyolite glass inclusion in quartz are shown in Figure 20. The sample was imaged at four different sample-to-detector distances: 30 mm, 100 mm, 150 mm, and 200 mm. The glass inclusion has a very similar absorption to quartz, and at 30 mm it is very difficult to distinguish the two materials. However, as the sample-to-detector distance increases, the phase contrast enhances dramatically the interface between the glass and quartz, making the inclusion easy to visualize. In
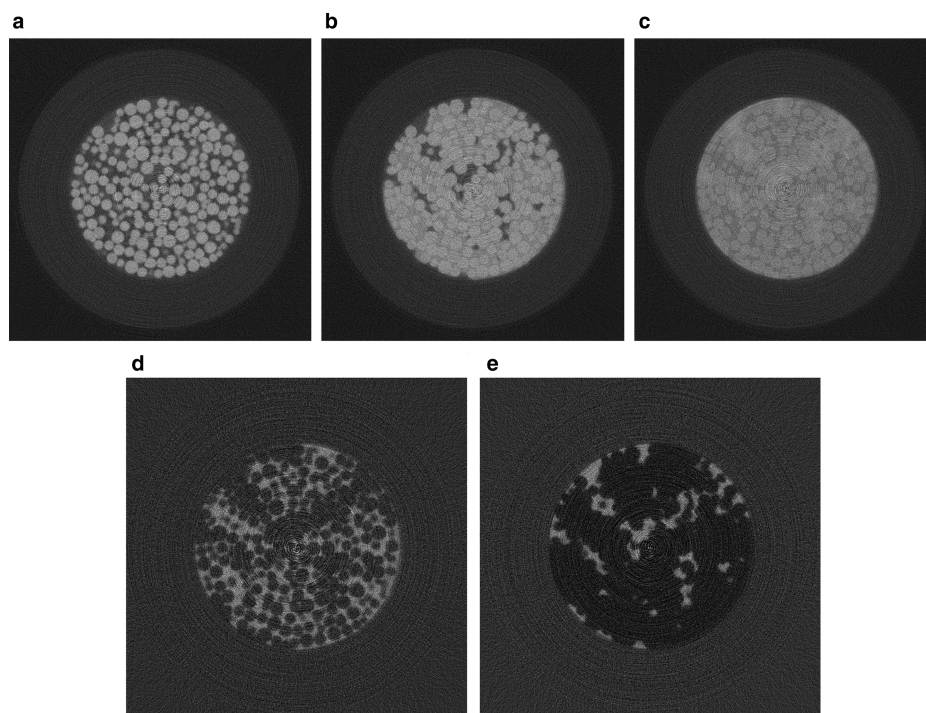
Figure 19. Reconstructed cross sections through an 8 mm-diameter column containing glass beads, an aqueous fluid with dissolved Cs and an organic fluid containing I. (a) Image collected at 32.5 keV, below both the I and Cs K absorption edges. (b) 33.2 keV, above the I edge but below the Cs edge. (c) 36.0 keV, above both the Cs and I edges. (d) Difference image 33.2–32.5 keV. (e) Difference image 36.0–33.2 keV.
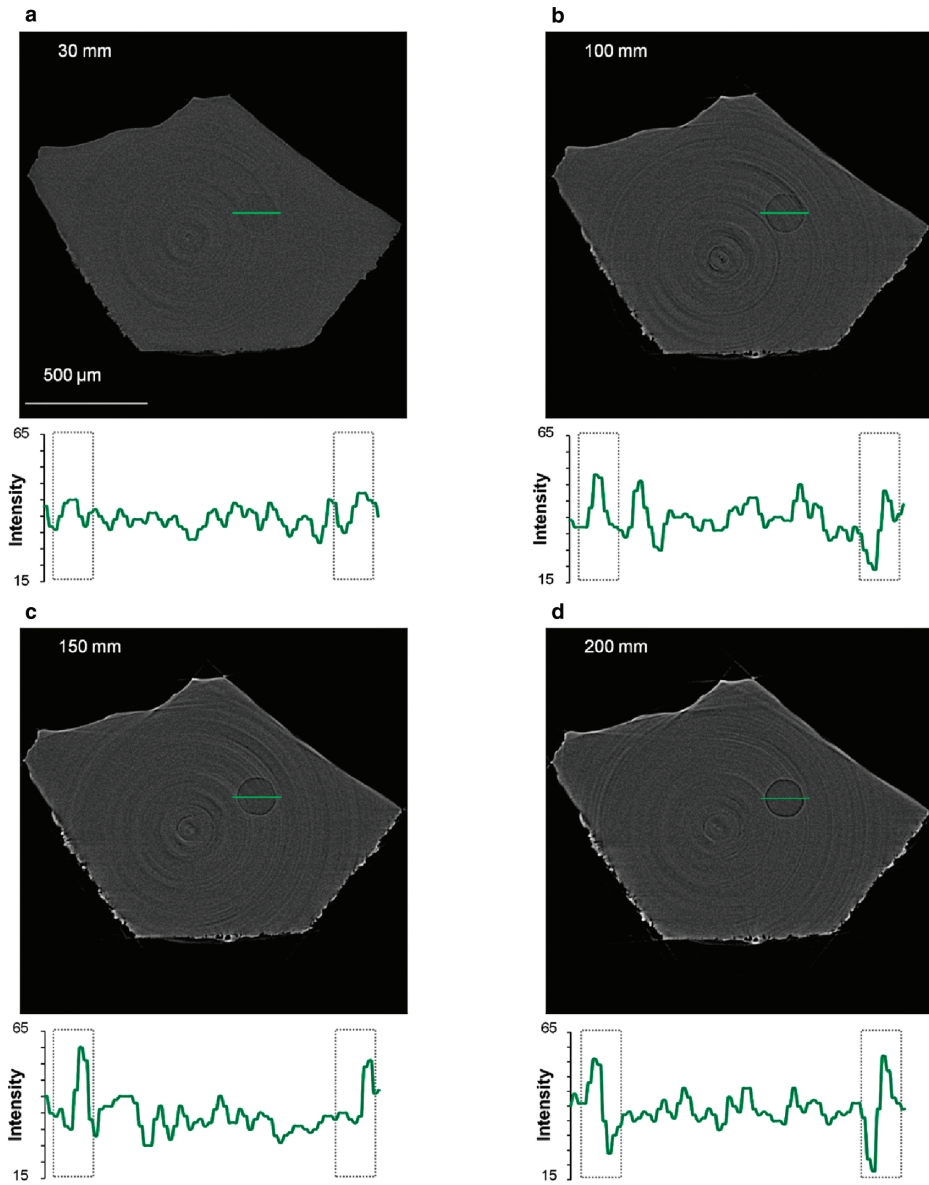
Figure 20. In-line propagation phase-contrast images of a rhyolite glass inclusion in quartz. Reconstruction cross sections imaged at sample-to-detector distances of 30 mm (a), 100 mm (b), 150 mm (c), and 200 mm (d). Intensity profiles across the green line through the inclusion are shown below each image.

some cases it is possible to quantitatively retrieve the phase information for the sample. This can improve the ability to segment images even when the absorption contrast is very small (Burvall *et al.*, 2011).

5. Fluorescence Tomography

X-ray fluorescence (XRF) provides a completely different contrast mechanism from X-ray absorption that has been discussed previously. X-ray fluorescence is very sensitive, so it permits measurement of elements that are present in extremely low concentrations, below the parts-per-million level. X-ray fluorescence requires detectors that can measure the energy of each X-ray they detect, with sufficient resolution to distinguish the neighboring elements in the periodic table. The fluorescence is produced by X-rays above the absorption edge of the element in question creating inner-shell electron vacancies, which are then quickly filled from outer-shells with the emission of a fluorescent X-ray. However, this fluorescence radiation is emitted in all directions. Because the radiation is emitted isotropically and because the fluorescence detectors have no position resolution, fluorescence tomography must be performed using first-generation techniques (Figure 1a, Figure 21). The incident X-ray beam is focused to a small diameter, typically using Kirkpatrick-Baez mirrors or zone plates. Beam diameters of a few microns or less are common. The sample is translated through the beam and the fluorescence radiation is collected, typically with the detector mounted at 90° to the incident beam to minimize X-ray scatter. The sample is then rotated a small amount, and the sample is translated again. Because the fluorescence detector is collecting all X-ray energies simultaneously, multiple elements in the sample are measured at the same time.
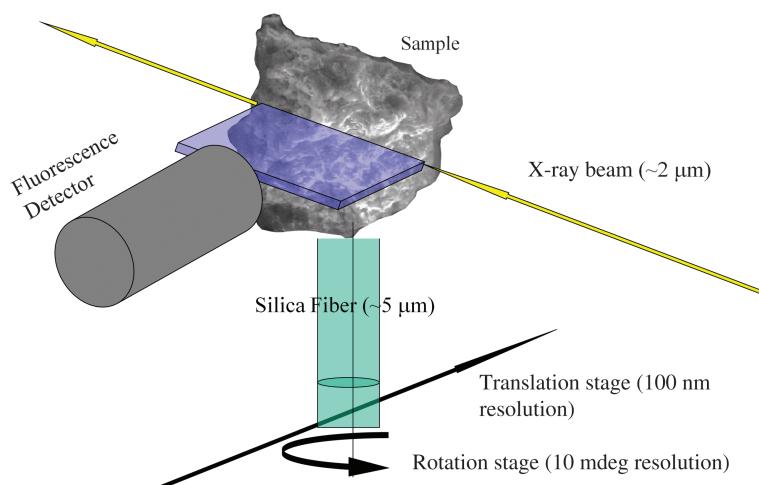

Figure 21. Schematic of fluorescence microtomography apparatus. This is a type of first-generation tomography (Figure 1a) but the detection is of the fluorescence X-rays rather than the transmitted beam.

Sinograms are constructed in the same manner as for absorption tomography above, except that the signal is the net counts in the fluorescence peak as a function of translation position (horizontal) and rotation angle (vertical). This signal is the line integral of the fluorescence along the beam through the sample. Ignoring absorption of the incident beam and absorption of the X-rays as they exit the sample, this is proportional to the concentration of the line integral of the concentration of the element along the beam path. The sinograms of FeKα, ZnKα, and AsKα measured in a cattail root from a contaminated site are shown in Figure 22 (Keon, 2002). These were collected by translating the sample 300 μm in 5 μm steps, and rotating the sample 180° in 3° steps. The reconstructions of the fluorescence tomography data for the elements shown in the sinograms (Figure 21) as well as Pb and Cu are shown in Figure 23. These images are 'virtual cross sections' of the root with a slice thickness of only 2 μm. An alternative way to collect such data would be to physically section the root and then make an X-Y XRF map. This would take the same number of measurements, but done in the X-Y plane rather than the X-θ plane. However, it would be very difficult to prepare a 2 μm thick section of such a sample, and it would have physically damaged the rest of the specimen. The fluorescence tomography cross-section thickness is limited only by the size of the X-ray beam rather than practical limits on physical sectioning.

The principal limitation of fluorescence tomography is X-ray absorption. The elements of interest are often low atomic number (K, Ca, Mn, Fe, *etc*.) and so have small absorption depths (Figures 2, 18). Absorption corrections can be made for both
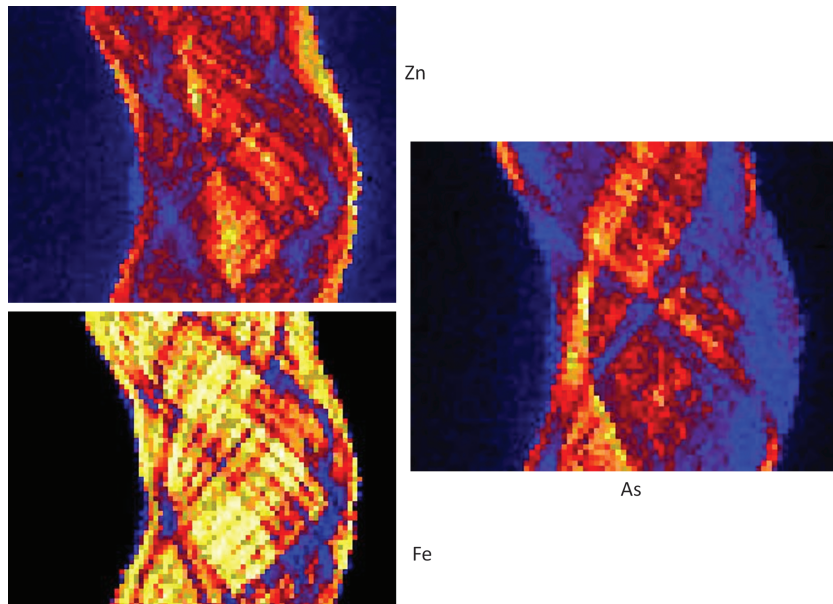

Figure 22. Fluorescence sinograms of Zn (upper left), Fe (lower left) and As (right). These were collected by translating the sample through 300 μm in 5 μm steps, and rotating the sample through 180° in 3° steps.
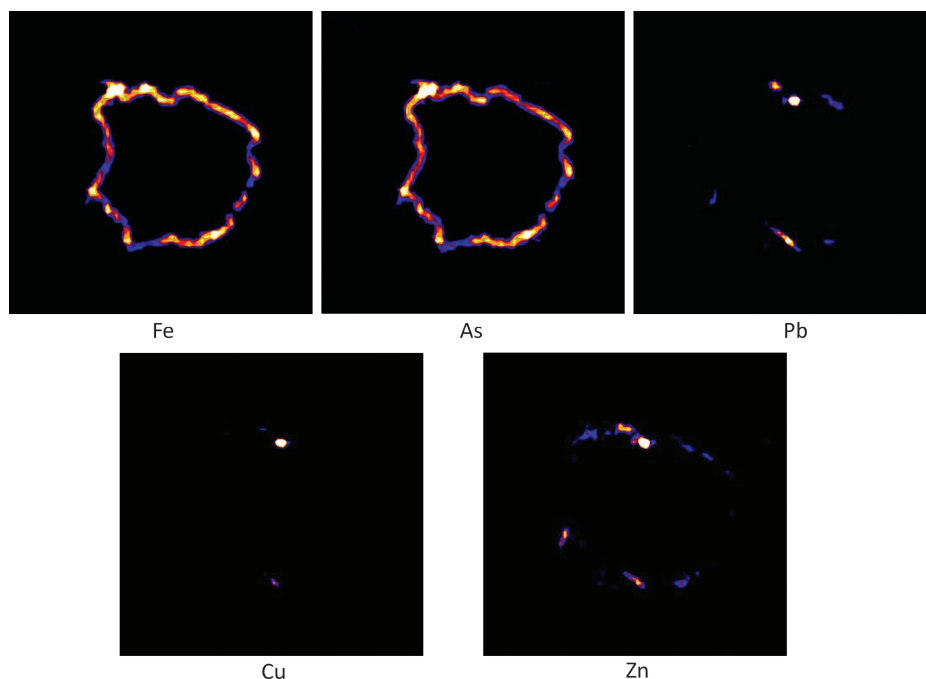
Figure 23. Reconstruction of the fluorescence tomography data for Fe (upper left), As (upper center), Pb (upper right), Cu (lower left), and Zn (lower right).

the incident beam and the fluorescent X-rays, but only up to maximum absorptions of 90% or so. This means that fluorescence tomography works best with relatively high-energy X-rays, small samples, and samples with a small mean atomic number. The technique thus works very well for transition elements in small biological samples, and the technique is commonly applied in this field.

6. Diffraction Tomography

Another type of signal that can be used in tomography is X-ray powder diffraction (Bleuet *et al.* 2008). This technique also requires first-generation tomography, because the powder diffraction detector measures the line integral of the diffraction intensity along the beam path with no spatial information. The reconstruction is of the intensity of a powder diffraction signal, which will correspond to the location of a single crystalline phase. This technique requires that the grain size be much less than the voxel size, so that good powder diffraction statistics are obtained from each voxel. The grains normally must not have strong preferred orientation, because the signal must be independent of the direction of the ray through a voxel. Finally the

sample–detector distance must be significantly greater than the sample diameter to prevent broadening of the diffraction lines due to different source points in the sample. The simultaneous X-ray diffraction (XRD) tomography and XRF tomography of a sample of bentonite clay is shown in Figure 24. The fluorescence detector was mounted at 90° to the incident beam, while the CCD diffraction detector was mounted near the 0° position downstream of the sample (Lanzirotti *et al.*, 2010). 1500 diffraction patterns were collected as a function of translation and rotation of the sample. The net intensities of the montmorillonite {001} and goethite {110} diffraction peaks were integrated using the *Fit2D* software. These intensities were converted into sinograms and reconstructed into cross-sections of the sample showing the distribution of these phases. The reconstructed distributions of Ni and Sr are also shown. The Ni is clearly associated with the goethite, while the Sr is located in the dark regions on the montmorillonite image, *i.e.* the regions that contain none of that phase. Diffraction tomography is not limited strictly to crystalline phases, but in some cases
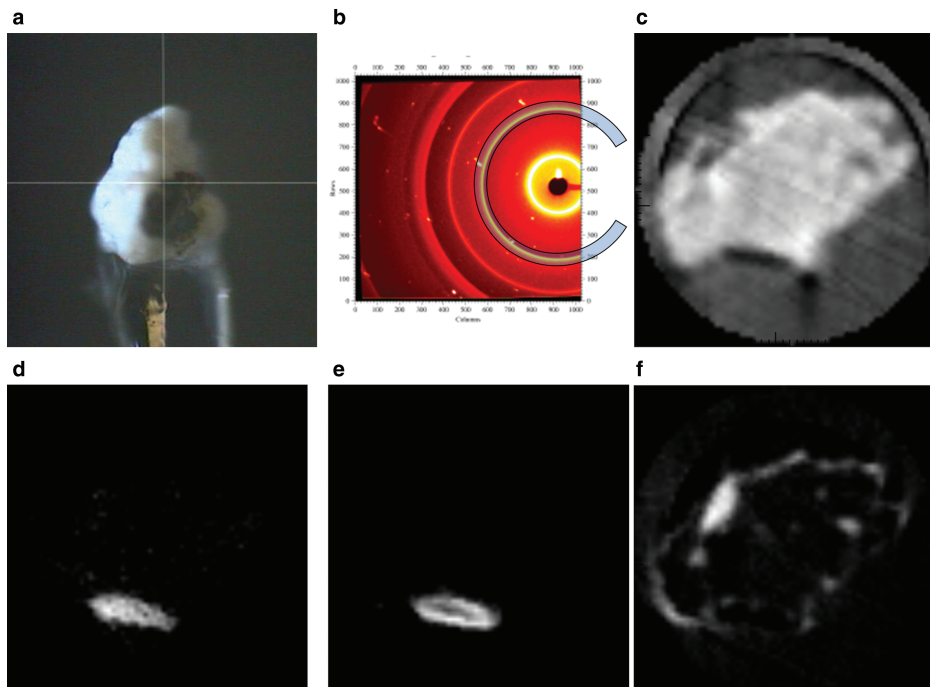

Q4

Figure 24. Simultaneous diffraction and fluorescence tomography of a bentonite clay sample. (a) Visible-light micrograph of clay sample mounted on silica glass fiber. The sample diameter is ∼200 μm. (b) Example XRD pattern from a CCD detector. The integrated intensity in a single X-ray reflection (*e.g.* montmorillonite {001}, shaded area) is computed using the program *Fit2D*. This intensity is used to form a sinogram from 1500 diffraction patterns measured as a function of sample translation and rotation. (c) Reconstruction of the location of the montmorillonite {001} diffraction. (d) Reconstruction of the goethite {110} diffraction. (e) Reconstruction of the Ni Kα fluorescence. (f) Reconstruction of the Si Kα fluorescence.

can be used to map the distribution of amorphous phases as well, *e.g.* in cement (Voltolini *et al.*, 2013).

7. Applications of Tomography in Earth Sciences

7.1. Fluids in porous media

Microtomography is becoming widely applied to studies of fluids in porous media. The use of synchrotron radiation and contrast agents has allowed visualization of the distribution of air-water systems (Armstrong *et al.*, 2012; Armstrong and Wildenschild, 2012; Wildenschild and Sheppard, 2013) and systems that also contain and organic fluid (Brusseau *et al.*, 2006, 2007, 2009; Narter and Brusseau, 2010). Such studies have application in enhanced oil recovery, groundwater remediation, and in generating input parameters to fluid dynamics models. Results from the Brusseau group where they initially saturated a sand column with an organic fluid are shown in Figures 25 and 26. The column was then repeatedly flushed with water in which the organic was sparingly soluble. The Brusseau group was able to study the details of the removal of the organic phase, the interfacial areas, *etc*. An important component of the groundwater environment is the presence of microbes.

Nanoparticles were used as contrast agents by Iltis *et al.* (2011) to image biofilms in wet porous media systems.
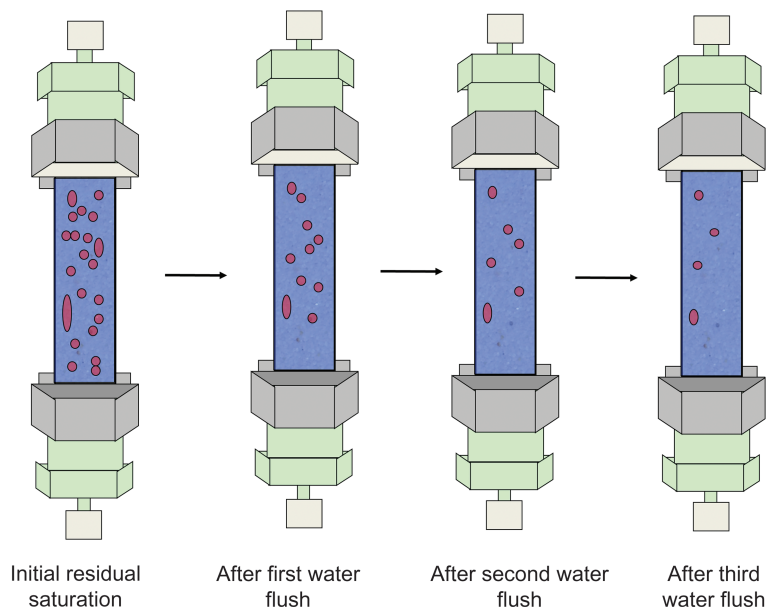

Initial residual After first water After second water After third
saturation   flush   flush   water flush

Figure 25. Cartoon showing sand initially saturated with an organic fluid, and then the organic distribution after successive flushes with water. The organic has a limited solubility in water.
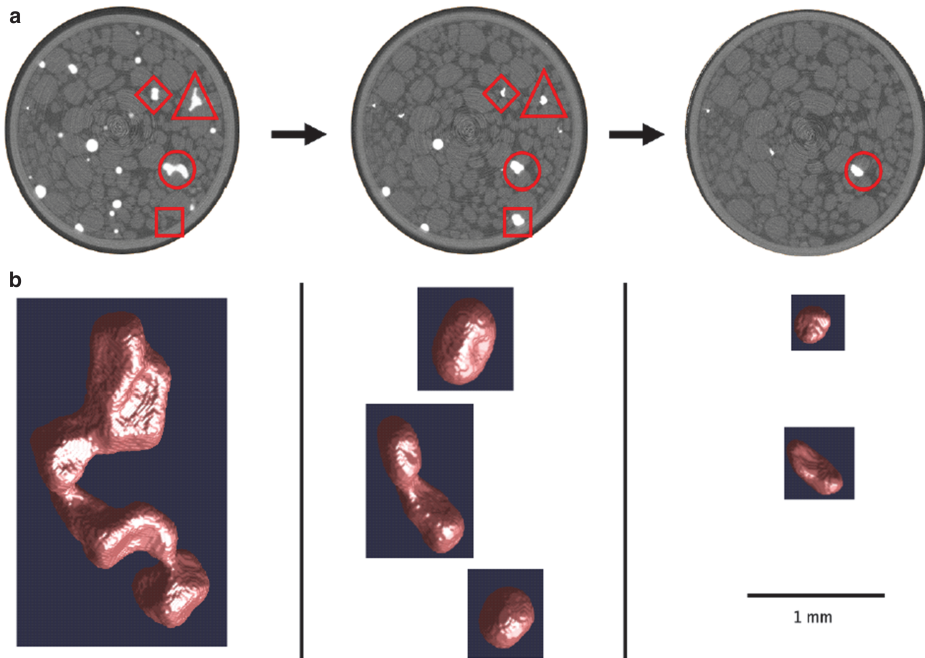
Figure 26. Reconstructed slices and 3-D renderings showing the distribution of organic fluid after successive flushings with water. The organic fluid is doped with iodine for contrast.

7.2. Soils

Microtomography is also finding wide use in the study of soil systems (Altman *et al.*, 2005; Crawford *et al.*, 2005; Feeney *et al.*, 2006; Anayeva *et al.*, 2013a, 2013b; Krave-chenko *et al.* 2011, 2013; Taina *et al.*, 2008; Wang *et al.*, 2012). For example Krav-chenko *et al.* (2013) used microtomography to follow the decay of organic carbon such as roots in soil aggregates in samples in both sterile samples and those with soil microorganisms.

7.3. Other applications

Microtomography is very useful in studying the internal structure of meteorites to learn about the early history of the solar system. Textures of the iron-nickel phases, collision events, porosity and other aspects have been studied (Ebel and Rivers, 2007; Friedrich *et al.*, 2008a, 2008b). Volcanic systems have been studied, both to learn about the process of vesicle formation in real time (Bai *et al.*, 2008; Baker *et al.*, 2012) and to study the distribution of trace-mineral phases by differential absorption tomography (Gualda *et al.*, 2010). *In situ* studies at high-pressure (Lesher *et al.*, 2009; Wang *et al.*, 2011) have been used to measure directly the volume of amorphous glasses and liquids, for which it is not possible to measure high-pressure density with XRD.

Finally both fluorescence tomography and differential absorption tomography have been used to study the distribution of trace metals in hyper-accumulating plants (McNear *et al.*, 2005; Scheckel *et al.*, 2007; Tappero *et al.*, 2007).

Acknowledgments

References

Altman, S.J., Rivers, M.L., Reno, M.D., Cygan, R.T., and McLain, A.A. (2005) Characterization of adsorption sites on aggregate soil samples using synchrotron X-ray computerized microtomography. *Environmental Science & Technology*, **39**, 2679–2685.

Ananyeva, K., Wang, W., Smucker, A.J.M., Rivers, M.L., and Kravchenko, A.N. (2013a) Can intra-aggregate pore structures affect the aggregate's effectiveness in protecting carbon? *Soil Biology and Biochemistry*, **57**, 868–875.

Ananyeva, K., Wang, W., Smucker, A.J.M., Rivers, M.L., and Kravchenko, A.N. (2013b) Intra-aggregate pore structures are related to total C distribution within soil macro-aggregates. *Soil Biology and Biochemistry*, **57**, 868–875.

Armstrong, R.T and Wildenschild, D. (2012) Microbial enhanced oil recovery in fractional-wet systems: a pore-scale investigation, *Transport in Porous Media*, **92**, 819–835.

Armstrong, R.T., Porter, M.L., and Wildenschild, D. (2012) Linking pore-scale interfacial curvature to column-scale capillary pressure. *Advances in Water Resources*, **46**, 55–62.

Bai, L., Baker, D.R., and Rivers, M.L. (2008) Experimental study of bubble growth in Stromboli basalt melts at 1 atm. *Earth and Planetary Science Letters*, **267**, 533–547.

Baker, D.R., Mancini, L., Polacci, M., Higgins, M.D., Gualda, G.A.R., Hill, R.J., and Rivers, M.L. (2012) An introduction to the application of X-ray microtomography to the three-dimensional study of igneous rocks, *Lithos,* **148**, 262–276.

Bleuet, P., Welcomme, E., Dooryhee, E., Susini, J., Hodeau, J.-L. and Walter, P. (2008) Probing the structure of heterogeneous diluted materials by diffraction tomography. *Nature Materials*, **7**, 468–472.

Brusseau, M.L, Peng, S., Schnaar, G., and Costanza-Robinson, M.S. (2006) Relationships among air-water interfacial area, capillary pressure, and water saturation for a sandy porous medium. *Water Resources Research*, **42**, W03501–W03505.

Brusseau, M.L., Peng, S., Schnaar, G., and Murao, A. (2007) Measuring air-water interfacial areas with x-ray microtomography and interfacial partitioning tracer tests. *Environmental Science & Technology,* **41**, 1956–1961.

Brusseau, M.L., Narter, M., Schnaar, G.J., and Marble, J. (2009) Measurement and estimation of organic-liquid/water interfacial areas for several natural porous media. *Environmental Science & Technology*, **43**, 3619–3625.

Burvall, A., Lundström, U., Takman, P.A.C, Larsson, D.H., and Hertz H.M. (2011) Phase retrieval in X-ray phase-contrast imaging suitable for tomography. *Optics Express.* **19**, 10359–10376.

Chapman, D., Thomlinson, W., Johnston, R.E., Washburn, D., Pisano, E., Gmür, N., Zhong, Z., Menk, R., Arfelli, F., and Sayers, D. (1997) Diffraction enhanced x-ray imaging. *Physics in Medicine and Biology*, **42**, 2015–2025.

Crawford, J.W., Harris, J.A., Ritz, L., and Young, I.M. (2005) Towards an evolutionary ecology of life in soil. *Trends in Ecology and Evolution*, **20**, 81–87.

Ebel, D.S. and Rivers, M.L. (2007) Meteorite 3-D synchrotron microtomography: Methods and applications. *Meteoritics and Planetary Science*, **42**, 1627–1646.

Feeney, D.S., Crawford, J.W., Daniell, T., Hallett, P.D., Nunan, N., Ritz, K., Rivers, M., and Young, I.M. (2006) Three-dimensional microorganization of the soil-root-microbe system, *Microbial Ecology*, **52**, 151–158.

Friedrich, J.M., Macke, R.J., Wignarajah, D.P., Rivers, M.L., Britt, D.T., and Ebel D.S. (2008a) Pore size distribution in an uncompacted equilibrated ordinary chondrite. *Planetary and Space Science*, **56**, 895–900.

Friedrich, J.M., Wignarajah, D.P., Chaudhary, S., Rivers, M.L., Nehru, C.E., and Ebel, D.S. (2008b) Three-dimensional petrography of metal phases in equilibrated L chondrites – Effects of shock loading and dynamic compaction. *Earth and Planetary Science Letters*, **275**, 172–180.

Gualda, G.A.R., Pamukcu, A.S., Claiborne, L.L. and Rivers, M.L. (2010) Quantitative 3D petrography using X-ray tomography 3: Documenting accessory phases with differential absorption tomography, *Geosphere* **6**, 782–792.

Iltis, G.C., Armstrong, R.T., Jansik, D.P., Wood, B.D., and Wildenschild, D. (2011) Imaging biofilm architecture within porous media using synchrotron-based X-ray computed microtomography. *Water Resources Research*, **47**, W02601-1–W02601-5.

Keon, N.E. (2002) Controls on arsenic mobility in contaminated wetland and riverbed sediments. Ph.D. thesis, Massachusetts Institute of Technology, Mass, USA.

Kinney, J.H. and Nichols, M.C. (1992) X-ray tomographic microscopy (XTM) using synchrotron radiation. *Annual Reviews of Materials Science*, **22**, 121–152.

Kravchenko, A.N., Wang, W., Smucker, A.J.M., and Rivers, M.L. (2011) Long-term differences in tillage and land use affect intra-aggregate pore heterogeneity. *Soil Science Society of America Journal*, **75**, 1658–1666.

Kravchenko, A., Chun, H.-C., Mazer, M., Wang, W., Rose, J.B., Smucker, A., and Rivers, M. (2013) Relationships between intra-aggregate pore structures and distributions of Escherichia coli within soil macro-aggregates. *Applied Soil Ecology* **63**, 134–142.

Lanzirotti, A., Tappero, R., Darrell G. Schulze, D.G. (2010) Chapter 2 - Practical Application of Synchrotron-Based Hard X-Ray Microprobes in Soil Sciences, In: *Developments in Soil Science*, **34**, (B. Singh and Markus Gräfe, editors), Elsevier, Amsterdam, pp. 27–72.

Lesher, C.E., Wang, Y., Gaudio, S., Clark, A., Nishiyama, N., and Rivers, M. (2009) Volumetric properties of magnesium silicate glasses and supercooled liquid at high pressure by X-ray microtomography. *Physics of Earth and Planetary Interiors*, **174**, 292–301.

Marinoni, N., Voltolini, M., Mancini, L., Vignola, P., Pagani, A., and Pavese, A. (2009) An investigation of mortars affected by alkali-silica reaction by X-ray synchrotron microtomography: a preliminary study. *Journal of Materials Science*, **44**, 5815–5823.

Mayo, S.C., Stevenson, A.W., and Wilkins, S.W. (2012) In-line phase-contrast X-ray imaging and tomography for materials science. *Materials* **5**, 937–965.

McNear, D.H. Jr., Peltier, E., Everhart, J., Chaney, R.L., Sutton, S., Newville, M., Rivers, M., and Sparks, D.L. (2005) Application of quantitative fluorescence and absorption-edge computed microtomography to image metal compartmentalization in Alyssum murale. *Environmental Science & Technology*, **39**, 2210–2218.

Momose, A., Takeda, T., Itai, Y., and Hirano, K. (1996) Phase-contrast X-ray computed tomography for observing biological soft tissues. *Nature Medicine*, **2**, 473–475.

Narter, M. and Brusseau, M.L. (2010) Comparison of interfacial partitioning tracer test and high-resolution microtomography measurements of fluid-fluid interfacial areas for an ideal porous medium. *Water Resources Research*, **46**, 1–7.

Rivers, M.L (2012) tomoRecon: High-speed tomography reconstruction on workstations using multi-threading, In: *Developments in X-ray Tomography VIII* (S.R. Stock, editor). Proceedings of SPIE, **8506**, pp. 85060U-1–85060U-13.

Rivers, M.L, Citron, D.T., and Wang, Y. (2010) Recent developments in computed tomography at GSECARS, In: *Developments in X-ray Tomography VII* (S.R. Stock, editor). Proceedings of SPIE, **7804**, pp. 780409-1–780409-15.

Scheckel, K.G., Hamon, R., Jassogne, L., Rivers, M., and Lombi, E. (2007) Synchrotron X-ray absorption-edge computed microtomography imaging of thallium compartmentalization in Iberis intermedia. *Plant and Soil*, **290**, 51–60.

Spanne, P. and Rivers, M.L. (1987) Computerized microtomography using synchrotron radiation from the NSLS. *Nuclear Instruments and Methods*, **B24/25**, 1063–1067.

Sutton, S.R., Bertsch, P.M., Newville, M., Rivers, M., Lanzirotti, A., and Eng, P. (2002) Microfluorescence and microtomography analyses of heterogeneous earth and environmental materials, In: *Applications of Synchrotron Radiation in Low-Temperature & Environmental Science* (xx and xx, editors). Reviews in Mineralogy & Geochemistry, **49.** Mineralogical Society of America, Washington, D.C, pp. 429–483.   **Q3**

Taina, I.A., Heck, R.J., and Elliot, T.R. (2008) Application of X-ray computed tomography to soil science: A literature review. *Canadian Journal of Soil Science*, **88**, 1–20.

Tappero, R., Peltier, E., Grafe, M., Heidel, K., Ginder-Vogel, M., Livi, K.J.T., Rivers, M.L., Marcus, M.A., Chaney, R.L., and Sparks, D.L. (2007) Hyperaccumulator Alyssum murale relies on a different metal storage mechanism for cobalt than for nickel, *New Phytologist*, **175**, 641–654.

Voltolini, M., Dalconi, M.C., Artioli, G., Parisatto, M., Valentini, L., Russo, V., Bonnin, A. and Tucoulou, R. (2013) Understanding cement hydration at the microscale: new opportunities from 'pencil-beam' synchrotron X-ray diffraction tomography. *Journal of Applied Crystallography*, **46**, 142–152.

Wang, W., Kravchenko, A.N., Smucker, A.J.M., and Rivers. M.L. (2012) Intra-aggregate pore characteristics: X-ray computed microtomography analysis. *Soil Science Society of America Journal*, **76**, 1159–1171.

Wang, Y., Lesher, C., Fiquet, G., Rivers, M.L., Nishiyama, N., Siebert, J., Roberts, J., Morard, G., Gaudio, S., Clark, A., Watson, H., Menguy, N., and Guyot, F. (2011) In situ high-pressure and high-temperature X-ray microtomographic imaging during large deformation: A new technique for studying mechanical behavior of multiphase composites, *Geosphere*, **7**, 40–53.

Waychunas, G.A. (2014) Introduction to synchrotron radiation, In: *Advanced Applications of Synchrotron in Clay Science* (G. Waychunas, editor). CMS Workshop Lecture Series, **19**, The Clay Minerals Society, Chantilly, Virginia, USA, pp. xx–xx.

Weitkamp, T., Diaz, A., David, C., Pfeiffer, F., Stampanoni, M., Cloetens P., and Ziegler, E. (2005) X-ray phase imaging with a grating interferometer. *Optics Express* **13**, 6296–6304.

Wildenschild, D. and Sheppard, A.P. (2013) X-ray imaging and analysis techniques for quantifying pore-scale structure and processes in subsurface porous medium systems. *Advances in Water Resources*, **51**, 217–246.

Wildenschild, D., Rivers, M.L., Porter, M.L., Iltis, G.C., Armstrong, R.T., and Davit, Y. (2013) Using synchrotron-based X-ray microtomography and functional contrast agents in environmental applications, In: *Soil–Water–Root Processes: Advances in Tomography and Imaging* (S.H. Anderson and J.W. Hopmans, editors), SSSA Special Publication **61,** American Society of Agronomy, Madison, Wisconsin, USA, pp. 1–40.